Journal of Colloid and Interface Science 676 (2024) 569–581

Contents lists available at ScienceDirect

Journal of Colloid And Interface Science

journal homepage: www.elsevier.com/locate/jcis

Surface-catalyzed liquid–liquid phase separation and amyloid-like assembly in microscale compartments

Giuseppe De Luca [a,b], Giuseppe Sancataldo [b], Benedetto Militello [b,c], Valeria Vetri [b,*]

[a] Department Biological, Chemical and Pharmaceutical Sciences and Technologies (STEBICEF), University of Palermo, Viale delle Scienze, 16, 90128, Palermo, Italy
[b] Department of Physics and Chemistry – Emilio Segrè, University of Palermo, Viale delle Scienze, 18, 90128, Palermo, Italy
[c] INFN Sezione di Catania, Via Santa Sofia 64, 95123 Catania, Italy

GRAPHICAL ABSTRACT

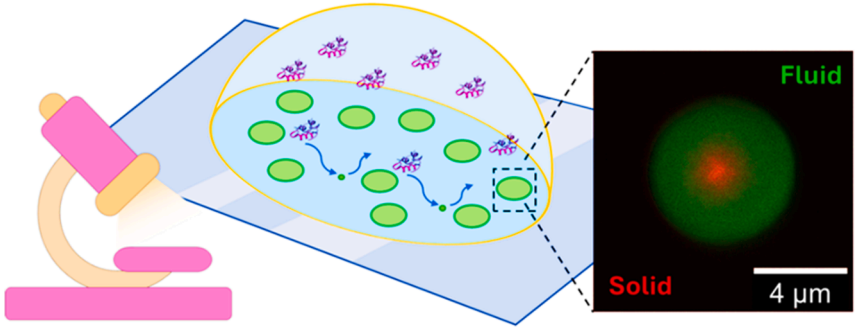

ARTICLE INFO

Keywords:
Liquid-liquid phase separation (LLPS)
Amyloid
Amyloid-like Superstructures
Human insulin
Surface catalysis
FLIM
Phasor analysis
Homogeneous nucleation

ABSTRACT

Liquid-liquid phase separation is a key phenomenon in the formation of membrane-less structures within the cell, appearing as liquid biomolecular condensates. Protein condensates are the most studied for their biological relevance, and their tendency to evolve, resulting in the formation of aggregates with a high level of order called amyloid.

In this study, it is demonstrated that Human Insulin forms micrometric, round amyloid-like structures at room temperature within sub-microliter scale aqueous compartments. These distinctive particles feature a solid core enveloped by a fluid-like corona and form at the interface between the aqueous compartment and the glass coverslip upon which they are cast. Quantitative fluorescence microscopy is used to study in real-time the formation of amyloid-like superstructures. Their formation results driven by liquid–liquid phase separation process that arises from spatially heterogeneous distribution of nuclei at the glass-water interface. The proposed experimental setup allows modifying the surface-to-volume ratio of the aqueous compartments, which affects the aggregation rate and particle size, while also inducing fine alterations in the molecular structures of the final assemblies.

These findings enhance the understanding of the factors governing amyloid structure formation, shedding light on the catalytic role of surfaces in this process.

* Corresponding author.
E-mail addresses: giuseppe.deluca04@unipa.it (G. De Luca), giuseppe.sancataldo@unipa.it (G. Sancataldo), benedetto.militello@unipa.it (B. Militello), valeria.vetri@unipa.it (V. Vetri).

https://doi.org/10.1016/j.jcis.2024.07.135
Received 19 April 2024; Received in revised form 24 June 2024; Accepted 16 July 2024
Available online 18 July 2024

1. Introduction

In recent years, liquid–liquid phase separation (LLPS) has gained increasing attention in both biological and biophysical research. LLPS involves the separation of a homogeneous solution into two phases: a denser, more concentrated phase retaining liquid-like properties, and a diluted phase depleted of most participating macromolecules [1–4]. In vivo, LLPS constitutes a fundamental phenomenon for the function of cells with a crucial role in health and disease: the condensation of proteins and other biomolecules, into liquid droplets is at the basis of the formation of subcellular membrane-less organelles [3,5,6]. In such structures, the macromolecule coacervates are in dynamic equilibrium with the environment due to the absence of any delimiting membrane [6]. Similar to the process of aggregation, the ability to LLPS can be considered a common property of protein molecules. Whether a protein solution undergoes phase separation depends on various factors, including the concentration of proteins in the solution and the specificity of their sequences [1,7–9]. Environmental conditions such as temperature, the type and concentration of salts, the presence of co-solutes, pH, and the volume excluded by other macromolecules play crucial roles in determining whether phase separation occurs [4,9–15].

Multivalent inter- and intra-molecular interactions have been found to drive the demixing from the homogeneous phase into a phase with different physico-chemical properties and characterized by lower free energy than the fully mixed state [2,16–18]. A balance of long-range and short-range forces regulates protein self-assembly into condensed states and weak interactions such as π–π stacking, van der Waals forces, hydrogen bonding and transient cross–β-contacts have been suggested to have a dominant role [3,10,17–19]. These forces are common to the ones involved in folding and aggregation but act in different extents. Notably, the dense phase that results from LLPS process represents a metastable state which may undergo a "maturation" process. It implies the stabilization of intermolecular bonds, leading to the development of a gel or solid-state structure [20,21,2,3,6].

The multiple underlying mechanisms of droplets maturation which may lead to protein aggregates or hydrogels are not clearly understood yet. In some instances, the LLPS of protein molecules was found also to involve the formation of cross β-structures [22,23,2,3]. Intermolecular hydrogen bonds, which are formed between neighboring β-strands, stabilize the supramolecular assemblies, and create a repetitive pattern of hydrogen bonding typical of amyloid structures. Thus, it is not surprising that in several instances LLPS phenomena were also found to be involved in amyloid structure formation [20,22–25]. Indeed, spherical liquid droplets were previously observed in the early stage of supramolecular assembly phenomena leading to fibrils formation [20,26–29]. More in general weak intermolecular H-bonds in the concentrated phase may increase their strength leading to a liquid-gel transition [24,30–33].

Amyloid structures themselves have been proposed to undergo LLPS to form dynamic structures as stress granules in cellular environment [3,5,34]. Moreover, amyloid structures can self-assemble in higher-order assemblies at a macroscopic or mesoscopic scale [35–37]. They may occur in various forms and sizes, including elongated fibrils [38], dense spherical microparticles (particulates) [39], and core–shell configurations with a dense, amorphous core surrounded by a fibril-like corona (spherulites) [40]. Importantly, these structures are generic and can be observed across various proteins and biological contexts. Despite their diversity, all these structures exhibit a common amyloid molecular structure, showcasing a regular pattern of intermolecular hydrogen bonds. The formation of these generic structures has been proposed to involve LLPS as the creation of spherical condensates enhances the interactions between protein molecules minimizing interfacial energy [41–44]. In general, protein supramolecular assembly involves multistep processes and interactions, as conformational changes (possibly including oligomer formation) and intermolecular bonding, nucleation mechanisms, phase transitions, etc [35,45–51]. Similar phenomena can be observed in the assembly routes of LLPS. Protein nucleation can be triggered by or trigger LLPS and these processes can occur either before or after oligomerization. The timing and progression of LLPS process may be regulated by external stimuli [3], including variations in temperature [13,52], ionic strength [10,53], or the presence of surfaces and interfaces [54].

Notably, surfaces and interfaces have been shown to catalyze amyloid formation [55–58] and more in general they can accelerate or slow down protein aggregation processes [25,59–61]. In vitro, the surface-volume ratio of the sample was found to be critical in regulating primary nucleation mechanism [59]. Adsorption of molecules at the interface can initiate supramolecular assembly inducing conformational changes or favoring the formation of nuclei [62].

In the presented study Human Insulin (HI) is employed as the model protein. This choice is motivated by extensive research conducted on it over the past decades regarding amyloid formation and its applications in the pharmaceutical field. HI is a relatively small hormone protein that may reassemble in different quaternary structures depending on physical and chemical parameters of the solution as pH, solvent composition, temperature as well as on insulin concentration [63–65]. In acidic conditions in acetic acid solution, the monomeric state is favored [63,65]. In such conditions, at high temperatures, the formation of amyloid fibrils and spherulites has been extensively studied and results show that a plethora of amyloid-like polymorphs can be formed with variations at the nano, micro or mesoscopic level [66–74]. Here we show a LLPS-driven process which coupled with a liquid-to-solid phase transition results in the spontaneous formation of amyloid-like self-assemblies. The selected experimental conditions enable the observation of the supramolecular assembly process within aqueous compartments ranging from nanoliters to hundreds of nanoliters. Monodisperse spherical particles displaying amyloid properties are generated at the solution-glass interface through homogeneous nucleation, originating from a spatially heterogeneous distribution of similar nuclei. These structures exhibit a solid core, and a liquid-like corona and display characteristics features that fall between protein particulates and spherulites.

Using quantitative fluorescence microscopy techniques, we were able to elucidate the different phases of these peculiar supramolecular assemblies. Specifically, by employing Thioflavin T (ThT), a gold standard fluorescent marker in amyloid research, we investigated the formation and growth of aggregates within sub-microliter compartments. The analysis of fluorescence lifetime of ThT using the phasor approach [68,75], revealed distinct structural characteristics of the newly formed species. Coupled with FRAP experiments, this approach allowed us to provide a thorough description of the entire process disentangling homogenous primary nucleation as a fundamental step of the formation. This study underscores the influence of surface-to-volume ratio on LLPS-driven processes within microscale compartments at interfaces, revealing a supramolecular assembly phenomenon that remains elusive in large-scale samples.

2. Materials and methods

2.1. Sample preparation and creation of aqueous compartment

Human Insulin (HI) was dissolved in a solution containing Acetic Acid 20 % and NaCl 0.5 M (pH=1.85). When completely dissolved, the solution of HI was filtered by a 0.2 μm filter and then diluted to a final concentration of 5 mg/ml. Protein concentration was measured by UV – Vis spectroscopy by means of a Jasco – V770 spectrophotometer using the molar extinction coefficient $\varepsilon = 1$ at 276 nm for 1.0 mg/ml. ThT and Tween 20 to a final concentration of 40 μM and 0.05 % w/v, respectively, were added to the solution. The stock concentration of ThT and Tween 20 are about two orders of magnitude higher (3.36 mM ThT and 5 % w/v Tween 20) with respect to the final concentration, to minimize the dilution effect and to make it negligible. For the experiment with HI labeled with Alexa 647 (HI647), it was added at the last step, at a final

concentration of 80 nM.

To create sub-microliter scale aqueous compartments a drop of a freshly prepared protein solution was injected in a 100 μl drop of mineral oil deposited on a glass coverslip using a standard pipette. A glass Hamilton syringe of 1 μl was used to inject the sample solution into the mineral oil drop. Before using the syringe, it was thoroughly rinsed with acetone and then with acetic acid. The initial five drops of the solution dispensed from the syringe were discarded. This procedure is employed to cleanse the syringe, removing undesired contaminants and any potential residues of acetone that might interfere with the aggregation process. Small aqueous droplets, with variable size, are immersed in the oil at the interface with the glass coverslip. Protein particles formation was observed within the microliter compartments either during measurements at the microscope stage or when the sample was incubated in the dark at lab temperature (23 °C). All the experiments were repeated at least three times.

2.2. Two-photon microscopy and confocal laser scanning microscopy

The experiments were performed using a Leica TCS SP5 confocal laser scanning microscope, with a 63×/1.40–0.60 and 40×/1.25–0.75 oil objective, and a scanning frequency 400 Hz (Leica Microsystems, Germany). All the images were acquired at a resolution of 1024 × 1024 pixels. ThT fluorescence was excited at 780 nm (Spectra-Physics Mai-Tai Ti:Sa ultra-fast laser) and the detection range was 450 – 600 nm for images acquired in two-photon microscopy mode. Kinetics measurements were acquired using two-photon excitation. For images acquired by confocal microscopy the ThT fluorescence was excited at 470 nm (Leica Supercontinuum White Light Laser (WLL)) with a detection range was 485 – 585 nm, and the HI647 fluorescence was excited at 633 nm (WLL) with a detection range is 650 – 750 nm. The analysis of the microscopy data was performed by the open-source software ImageJ Fiji (https://imagej.net/software/fiji/).

2.3. Fluorescence lifetime imaging microscopy (FLIM)

Fluorescence lifetime imaging measurements (FLIM) were acquired in the time domain by means of a Leica TCS SP5 confocal laser scanning microscope coupled with picoHarp 300 TCSPC module (Picoquant, Germany). 256 × 256 pixels FLIM images were collected with a 63×/1.4 oil objective and scanning frequency 400 Hz, exciting ThT fluorescence at 470 nm (WLL) and collecting it in the detection range 485 – 585 nm (laser repetition rate is 80 MHz).

2.4. FLIM phasor plot analysis and interpretation

FLIM data were analyzed by phasor approach, described for the first time by Digman and colleagues [75]. Phasor analysis is a technique that enables a graphical representation of FLIM data. It involves mapping the fluorescence decay data obtained at each pixel of an image into a polar plot, known as a phasor plot, through Fourier transform. The phasor plot consists of two coordinates, g and s, which are respectively the real and imaginary parts of the Fourier transform of the measured fluorescence decay. In this analysis, a single exponential lifetime decay lies on the "universal circle," a semicircle with a radius of 0.5 and centered at the point with coordinates (0.5; 0). This semicircle extends from the point (1; 0), where shorter lifetimes ($\tau = 0$) are mapped, to the point (0; 0), where longer lifetimes ($\tau = \infty$) are mapped. Multi-exponential decays fall within the universal circle because phasors respect vector algebra rules. Specifically, a two-component lifetime decay aligns with a straight line that connects the two individual lifetime components of the complex decay. Furthermore, the distance of a phasor point on the line from one of the two single components (normalized to the total length of the chord) is the weight of the other single component in the complex lifetime, and vice versa. The weights are often referred to as a fraction.

To have a spatial localization of the fluorescence lifetime distributions obtained in the phasor plot, phasor distributions can be selected using colored cursors. As result, all the pixels of the original image, associated with the phasors selected by the cursor, will be colored with the same color of the used cursor, obtaining a new image in false colors called "phasor map". For a two components lifetime, known the two single components, it is possible to analyze the data and to obtain the map of the fraction of the first component, therefore providing overall information of the lifetime with a higher spatial resolution. The resulting image has a continuous color code, and it is called "fraction map".

FLIM analysis was performed by the SimFCS4 software developed at the Laboratory of Fluorescence Dynamics, University of California at Irvine (https://www.lfd.uci.edu). FLIM calibration of the system was performed by measuring the fluorescence lifetime of Fluorescein in a basic aqueous solution that is known to be a single exponential of 4.0 ns.

2.5. Fluorescence recovery after Photobleaching (FRAP)

FRAP experiments were performed using FRAP wizard of the Leica TCS SP5 confocal laser scanning microscope control software and WLL as an excitation/bleaching source. The 256 × 256 pixels images were acquired with a 63×/1.4 oil objective, and scanning frequency 400 Hz, on the samples that present a fraction of HI647 (80 nM). HI647 fluorescence was excited at 633 nm (Leica "white light" laser) and collected photons in the range 650 – 750 nm. Bleaching was performed for 20 frames (1.306 exposure time per frame) with high laser power in a circular region of interest with a radius of about 1 – 1.2 μm. The analysis of the microscopy data was performed by the open-source software ImageJ Fiji (https://imagej.net/software/fiji/).

3. Results and discussions

3.1. HI particles in sub-microliter volume

To monitor the growth of protein assemblies we performed experiments on sub-microliter scale sample drop (SD) containing Human Insulin aqueous solution. This allowed us to analyze, in real-time, the kinetics and growth of microscale protein assemblies by means of fluorescence microscopy methods.

Fig. 1a) and b) depict schematic representations of the experimental setup from both a top view and a side view perspective. A sub-microliter volume SD (yellow circle/hemisphere) was injected into a 100 μl mineral oil drop (grey circle/hemisphere) cast on a microscopy grade glass cover slip, and the fluorescent insulin microparticles (green circles/semicircles) on the interface between the glass coverslip and the aqueous SD. The sample contains 5 mg/ml HI in a 20 % Acetic acid solution (pH 1.85), 0.5 M NaCl and 0.05 % Tween 20.

As previously reported, the presence of Tween 20 favors the formation of stable aqueous compartments, well defined in shape and encapsulated within the oil [76–78]. This non-ionic water-soluble amphiphilic surfactant has great compatibility with protein molecules and at the chosen concentration, stabilizes the water/oil interface avoiding water-in-oil leaking effects [77,79]. In Fig. 1c) we report a representative 1024 × 1024 pixels two-photon microscopy image (λ_{exc} = 780 nm, detection range = 450–600 nm) of Thioflavin T (ThT) stained sample after about 5 h from the deposition, the profile of the aqueous SD ((250 ± 10) μm diameter) is highlighted using a yellow circle. Representative measurements at a higher spatial resolution of different SDs of the same size, in the same experimental conditions, are reported in panels d) and e). As observed, nearly spherical particles, characterized by uniform sizes with minimal variation from one another, are evenly dispersed within the SD, with an average diameter of approximately 5 μm. Importantly, by exploring the entire volume of several aqueous SD, our data suggest that these particles exclusively developed near the bottom of the SD, in proximity to the glass coverslip surface, with a random distribution across the surface. Notably, as mentioned above,

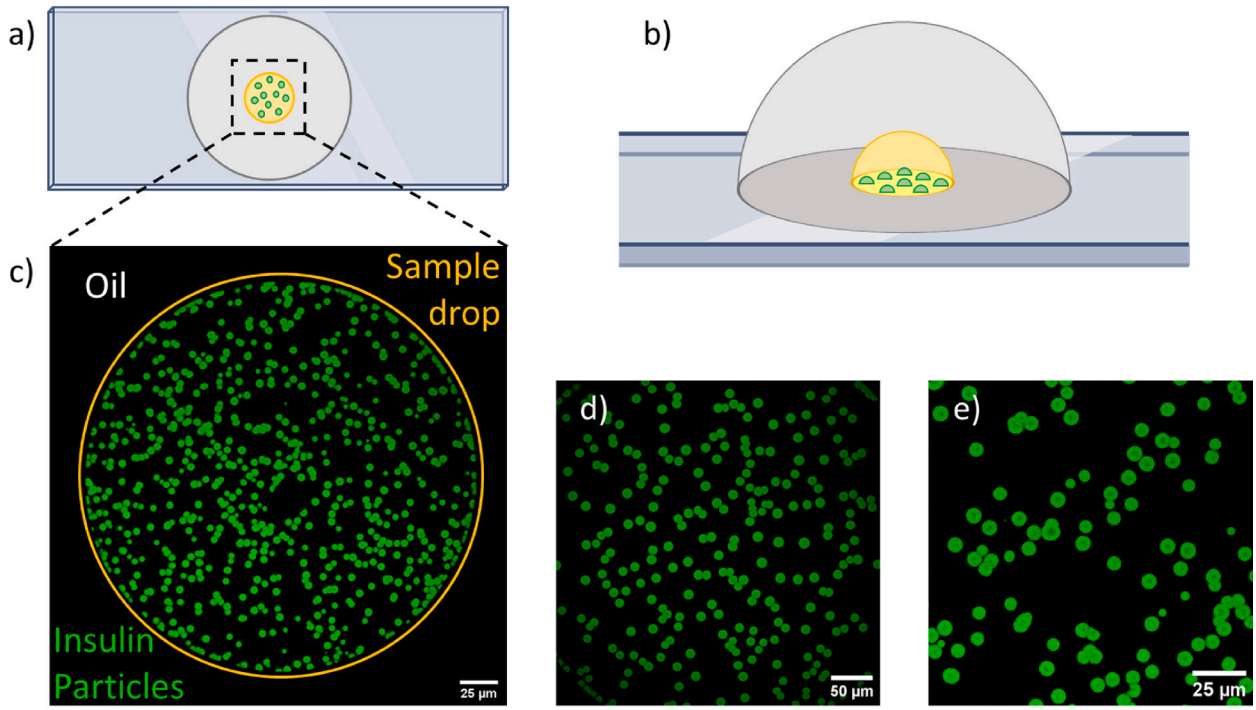

Fig. 1. (a) Top-view and (b) three-dimensional side-view representations (not in scale) of the experimental setup diagram: an aqueous SD (depicted as a yellow circle/hemisphere) is injected into a mineral oil drop (grey circle/hemisphere) on a glass cover slip. Protein assemblies grow at the bottom of the aqueous SD (small green circles/semicircles). (c) A representative two-photon microscopy fluorescence image (1024 × 1024 pixels) of the aqueous SD (outlined in orange) within the oil. The HI particles form by incubating 5 mg/ml HI in a 20 % acetic acid solution (pH 1.85), 0.5 M NaCl, 0.05 % Tween 20, and 40 μM ThT at room temperature for approximately 5 h in a 250 μm SD. A scale bar of 25 μm is provided. (d-e) Representative two-photon microscopy fluorescence images (1024 × 1024 pixels) of analogous samples in repeated experiments at different spatial resolutions. Spherical particles exhibiting positive ThT staining consistently exhibit similar morphology. The measured fluorescence intensity tends to be lower in the central region of these particles.

the experimental conditions also include Tween 20 as an amphiphilic agent to stabilize the aqueous compartment. Our data do not allow for the specific localization of Tween 20 within the drop. However, since its concentration is above the critical micellar concentration [80,81], it can be inferred that this surfactant is distributed both in bulk and at the interfaces. As shown, protein supramolecular assemblies positive to ThT exclusively at the glass surface and no diffusing species are observed in bulk solution or at the water–oil interface. This suggests a preferential role of the water–glass interface in the formation of these structures.

The observed fluorescence signal is due to the presence of ThT staining, a widely recognized fluorescent dye extensively employed for the identification and analysis of amyloid structures. ThT is particularly valuable in highlighting key stages of supramolecular assembly during amyloid formation, ranging from liquid-liquid phase separation (LLPS) events to the development of mature intermolecular β-structures [20,33,82–84]. Noteworthy, the fluorescence signal is not homogeneous within the particles. Specifically, the fluorescence signal is lower in the central part resulting in the presence of a darker core region (in Fig. 1e). The lack of fluorescence observed in the central region, located at the equatorial plane of these small particles, can be ascribed to various factors; among them the existence of an internal cavity within the particles, the limited affinity of ThT for the particle core, or the restricted accessibility of ThT molecules to the internal regions of the particles. We have previously observed low ThT fluorescence intensity in the core of HI spherulites, which we were able to correlate with a high density of native protein in the core of these structures [68].

To acquire additional information on the structure of the HI microparticles, we conducted an analogous experiment to the one described above, adding HI covalently labeled with Alexa 647 (from now on HI647) to the solution. HI647 concentration is 80 nM, resulting in a molar ratio $1{:}10^4$ between labeled and unlabeled molecules: the same spherical fluorescent particles were observed to form in the sample on the same timescale. Interestingly, higher Alexa 647 fluorescence intensity was measured in the central part of the microparticles (see Figure S1).

In Fig. 2, results of Fluorescence Recovery After Photobleaching (FRAP) experiments on the particles are reported. These measurements are aimed at investigating the mobility of HI molecules within protein particles. Fig. 2a-c) shows representative 1024x1024 confocal microscopy fluorescence images of particles grown in a 330 μm (diameter) SD, containing HI647. Images were acquired in two channels, green and red. The green channel in Fig. 2a) shows ThT fluorescence (λ_{exc} = 470 nm, detection range = 485–585 nm). Alexa 647 fluorescence is shown in the red channel in Fig. 2b) (λ_{exc} = 633 nm, detection range = 650–750 nm). The signals of ThT and Alexa 647 are overlapped in Fig. 2c), showing the two channels merged. In Fig. 2d) a representative 1024x1024 two-photon microscopy fluorescence image of the particles obtained incubating HI overnight in a 300 μm is shown.

ThT staining allows detecting the presence of spherical structures with an average diameter of about 5 μm. As shown in Fig. 2a) and d) and in line with results in Fig. 1 these structures exhibit lower ThT fluorescence intensity in the central region. To better visualize the intensity profile of ThT fluorescence measured along the diameter (yellow dashed line) of one particle is shown (green line) to highlight the reduced fluorescence in the core. As evident from the data reported in Fig. 2b), the intensity of Alexa 647 is notably higher in the central region of the spherical particles. This observation suggests that HI molecules accumulate within the core of the particles. Higher density of protein is found compared to the external portion, where a lower ThT signal is detected (Fig. 2c). This is more evident in Fig. 2e) where the magnification of a single particle image is shown in the red channel. Purple and orange circles are used to highlight two representative ROI (radius ~1.2 μm) in the core and the edge of the particles respectively where FRAP experiments were performed.

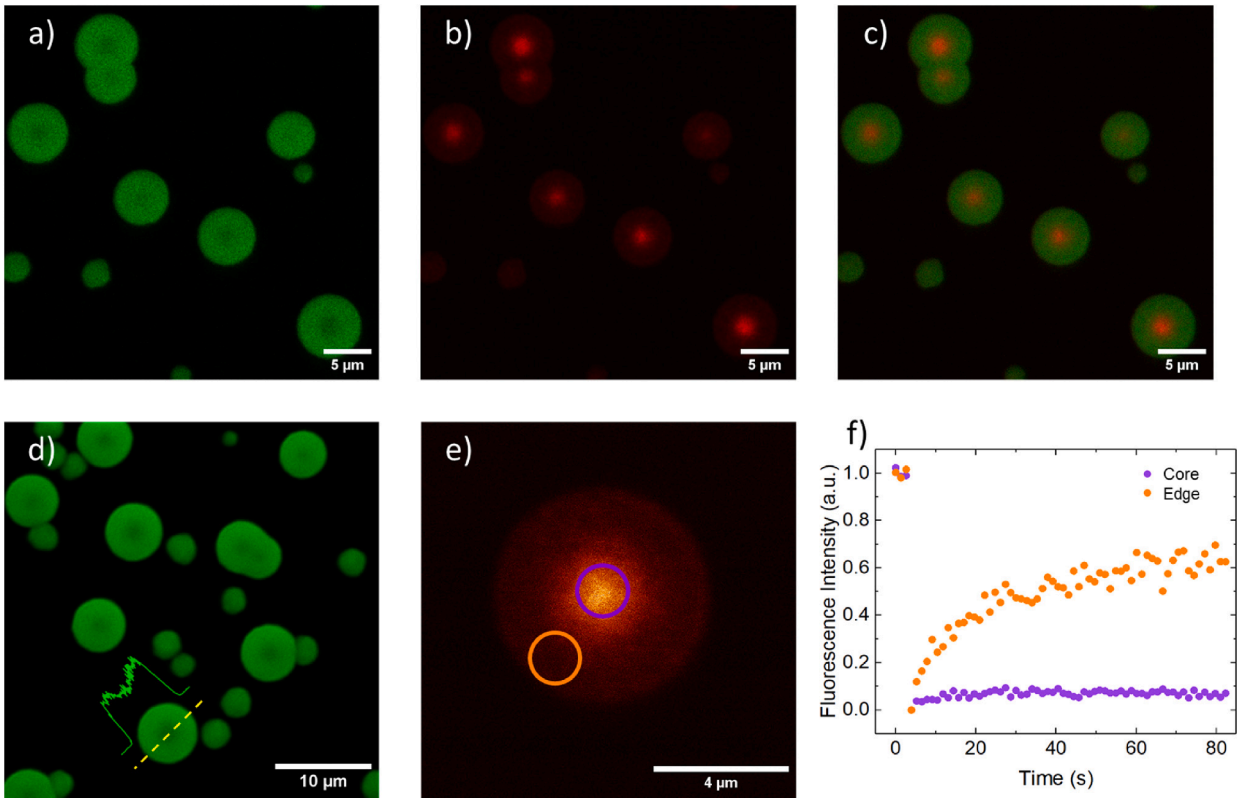

Fig. 2. (a-c) 1024 × 1024 pixels representative fluorescence confocal microscopy images in two channels of HI particles obtained incubating at room temperature overnight 5 mg/ml HI and HI647 80 nM in a 20 % Acetic acid solution (pH 1.85), containing 0.5 M NaCl, 0.05 % Tween 20 and 40 mM ThT in a 330 µm SD. HI647 is present in the sample with a molar ratio $1{:}10^4$ ratio with respect to HI. a) ThT fluorescence is shown in the green channel (λ_{exc} = 470 nm, detection range = 485–585 nm). b) Alexa 647 fluorescence is shown in the red channel (λ_{exc} = 633 nm, detection range = 650–750 nm). c) Merged image showing the fluorescence of ThT and Alexa 647 in the same color code. d) Two-photon microscopy fluorescence image of the HI particles stained with ThT incubated overnight in a 300 µm SD. Lower fluorescence intensity is detected in the core of each particle. The green line represents the intensity profile of ThT fluorescence measured at the yellow dashed line. e) Magnification of a single structure in the red channel. The purple and the orange circles are used to select typical regions (radius ~1.2 µm) where bleaching was performed in FRAP experiments. f) Fluorescence intensity recovery as a function of time in ROIs in the core (purple dots) and at the edge of the HI condensates (orange dots). Fluorescence Intensity is normalized to the average intensity measured in the ROI before photo-bleaching.

The fluorescence intensity recovery is reported as a function of time in Fig. 2f) for the two ROIs. Data are normalized to the average fluorescence intensity within the ROI before the bleaching. As can be seen, after photo-bleaching, the fluorescence intensity signal measured at the edge of the particle increases to a plateau in about 80 s. The signal recovery is about 60 % of the initial signal, so an immobile fraction of about 40 % can be estimated. On the contrary, no significant fluorescence recovery is measured in ROI at the core of the particles.

These observations can be explained considering that the observed HI supramolecular structures are constituted by a central compact core where proteins are in an immobile state, due to a rigid environment, which may reflect a solid, gel or highly viscous state, surrounded by a region where HI proteins have a larger mobility indicating that HI molecules are able to diffuse in a fluid-like matrix. The solid nucleus at the core of the observed protein condensates shows a lower affinity for ThT. This indicates a different molecular structure in this region with respect to the one in the external part similar to what was previously reported for HI spherulites formed at high temperature and in bulk experiments [68]. The fact that the outer region of the observed protein particles is in a fluid-like state, together with the spherical shape of the newly formed structures, indicates liquid–liquid phase separation as an underlying mechanism of the formation of these liquid-like condensates with a solid core.

3.2. Formation and evolution of supramolecular assemblies

By collecting images at regular time intervals after SD deposition, we were able to monitor the aggregation kinetics in situ within the submicroscale SD. Representative fluorescence microscopy images of events occurring in a 260 µm diameter drop as a function of time are reported in Fig. 3. The time-lapse Video is reported in the supplementary materials (see Video1). In the initial stages (about 2.5 h) a lag phase is observed where no significant ThT fluorescence signal is measured; afterward, almost simultaneously (within 10 – 15 min), fluorescence intensity starts growing from small and fixed spots (nucleation points) close to the coverslip glass surface. The fluorescence intensity increases abruptly, while the size of the particles grows with a radial symmetry until an equilibrium is reached. Once the size is stabilized the fluorescence intensity remains constant over time. Within the spatial resolution of the measurements, no diffusing species are detected, and it is possible to note that protein particles grow radially from a nucleation point in the center corresponding to the solid native-like core of the condensate found at the end of the kinetics.

The time evolution of the supramolecular assembly can be retrieved by measuring the ThT fluorescence intensity over time, in various Regions of Interest (ROIs) of the image. ThT intensity can be quantified at multiple levels including the entire SD, individual particles, or even specific regions within the particles, down to the resolution of single pixel. This comprehensive approach allows for a detailed examination of how ThT fluorescence evolves at different spatial scales throughout the assembly process.

In Fig. 4a) we report a 1024 × 1024 pixels two-photon microscopy fluorescence image of a 260 µm diameter SD after the formation of HI particles, after about 16 h of incubation at room temperature. Magnified

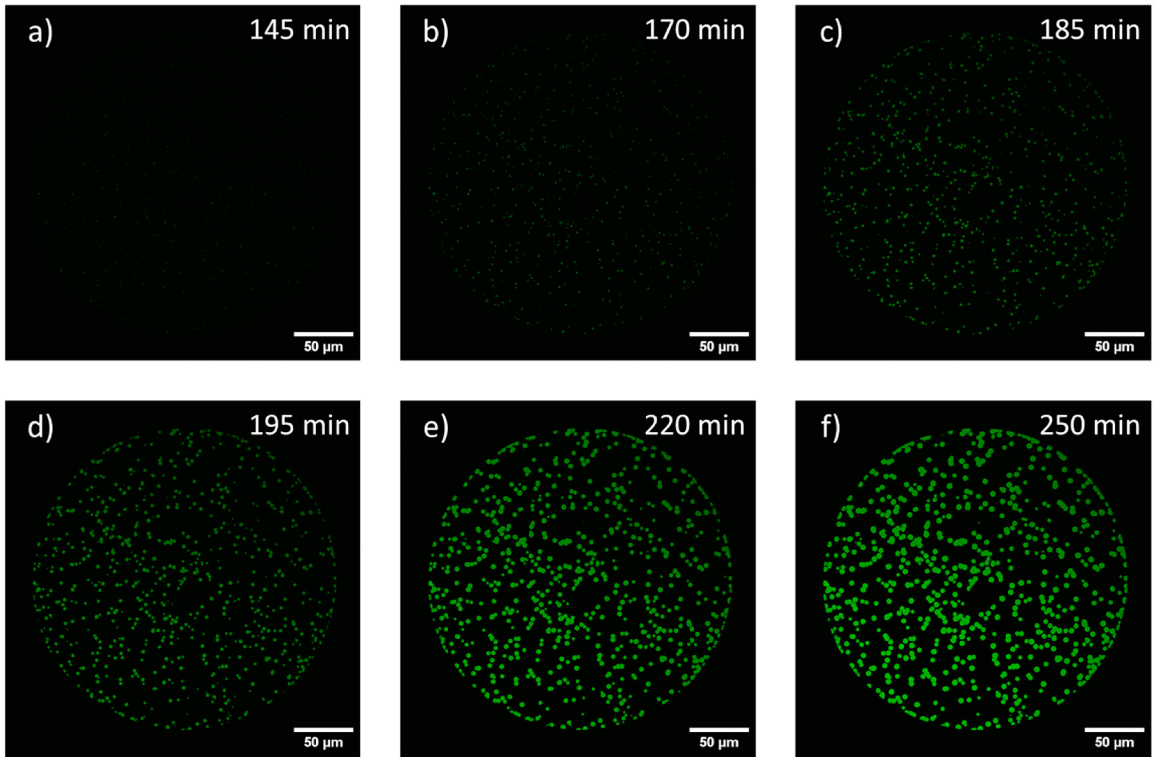

Fig. 3. Representative fluorescence microscopy images of events occurring as a function of time when a 5 mg/ml HI in a 20 % Acetic acid solution (pH 1.85), 0.5 M NaCl, 0.05 % Tween 20 and 40 mM ThT is incubated at room temperature for 6.4 h in a 260 µm SD. Images at different time points are shown: a) 145 min, b) 170 min, c) 185 min, d)195 min, e) 220 min, and f) 250 min. The time-lapse video is reported in the supplementary materials (see Video1).

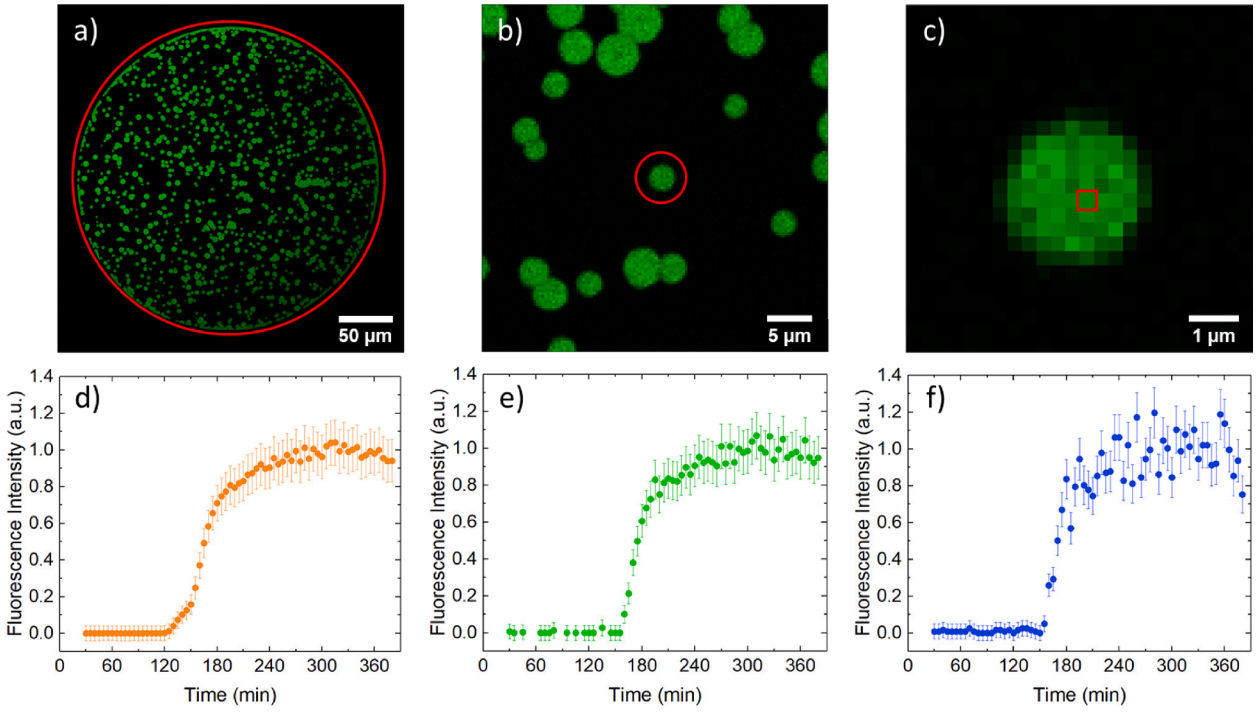

Fig. 4. (a) 1024 × 1024 pixels two-photon microscopy fluorescence image of HI particles within an aqueous SD with 260 µm diameter (λ_{exc} = 780 nm, detection range = 450–600 nm). Scale bar is 50 µm. (b – c) Magnification of details in the image in panel (a). A SD of 5 mg/ml HI dissolved in a 20 % Acetic acid solution (pH 1.85, containing 0.5 M NaCl, 0.05 % Tween 20 and 40 mM ThT), is injected in a 50 µl mineral oil and the sample is incubated at room temperature on the microscope stage during time-lapse measurements. Image stacks are acquired at regular time intervals and ThT fluorescence intensity is monitored in single ROIs with different sizes highlighted in red. (d – f) Normalized ThT fluorescence intensity versus time, obtained by integrating in each frame the values of every pixel of the ROI, neglecting the one with a value under 5, to eliminate the contributions of free ThT in solution. The kinetics has a sigmoidal profile with a lag phase, growth phase and plateau phase.

areas of this measurement are reported in panels b) and c). ThT fluorescence intensity was measured as a function of time in the red ROIs. ThT fluorescence time evolution in the different ROIs is reported in panel d) for the entire SD, e) for a single particle, and f) for a pixel within the particle. Fluorescence intensity is normalized to the maximum value reached at the equilibrium. All observed kinetics exhibit a characteristic sigmoidal shape, typical of nucleated processes, featuring a lag phase of approximately 150 min followed by a growth phase lasting 100 min, reaching a plateau phase thereafter. The kinetics profile of the ThT fluorescence measured in a single particle (Fig. 4e) and at a single point within the particles (Fig. 4f) resemble the kinetics measured in the entire SD, with an expected decrease of the signal-to-noise ratio due to the reduction of ROIs' size.

ThT fluorescence intensity kinetics were measured for various particles and in diverse regions within individual particles, revealing analogous profiles within the same sample, indicative of an ergodic behavior. Under the observed conditions, it is possible that nucleation at the bottom of the SD at the solution-glass interface serves as the initial stage of new phase formation. The initial formation of small clusters or "seeds" of a different protein phase triggers the growth of a new liquid dense phase.

It is worth noting that HI is often used as a model protein [37] for amyloid aggregation studies and that, in analogous solution conditions, amyloid formation was extensively studied in bulk with typical volumes from tens or hundreds of microliters up to milliliters at temperatures well above 50 °C [37,59,61,67–73,85]. The sample holder volumes reported in the literature are at least one magnitude order larger with respect to the ones explored here. As a reference, in the approximation of SD as spherical hemispheres, the volume of a 250 μm diameter SD is about 2 nl. Larger SDs present volumes ranging between tens and few hundreds of nanoliters; these volumes critically differ from the one used in standard plate readers. We have performed control experiments at room temperature, for the very same HI solution, in milliliter scale sample volumes in cuvette. In these conditions, supramolecular assembly is not observed for up to 48 h (see Figure S2). It is well known in the literature that, at high temperature and in acidic conditions, HI forms amyloid fibrils or spherulites following mechanisms regulated by heterogeneous nucleation [66,67,71]. In the conditions reported in literature, insulin supramolecular assembly at high temperature is known to be regulated by secondary nucleation mechanisms. Aggregation occurs following several steps which include a stochastic formation of the stable aggregates both in bulk and at the surface which trigger further aggregation. This results in both spatial and temporal heterogeneity of the aggregation kinetics and in multiple and diversified aggregate species within the same sample. In the presented conditions data clearly show that the protein supramolecular assemblies form only at the solution-glass interface, from heterogeneously distributed nuclei. Aggregates growth is characterized by analogous ThT fluorescence kinetics profiles. Furthermore, the newly formed supramolecular assemblies are homogeneous in size and shape within the same samples. This suggests that homogeneous mechanisms are involved in the onset and maturation of these structures.

3.3. Effect of sample drop size in the supramolecular assembly

With the idea of exploring the role of sample size in the observed HI supramolecular assembly we report in Fig. 5a) the ThT fluorescence intensity kinetics in five different SDs, prepared using the very same protocol but with different diameters which range from about 130 μm to 1500 μm.

The observable under consideration is the ThT fluorescence intensity, measured over time across the entire SD. The obtained kinetics data are normalized to the final fluorescence intensity value in the plateau region. Consistent with the observations reported in Fig. 4, the growth of fluorescence intensity exhibits a sigmoidal profile in all the measured samples. Notably, this process is more rapid in smaller-sized SDs. The kinetics profile reveals a critical correlation with SD size, with larger SDs exhibiting a longer lag phase before observable changes occur. In panel 5b) the same kinetics are reported after being offset to match the duration of the lag phase, thereby allowing the growth profiles to overlap, and in Fig. 5c) the aggregation rate, measured as the inverse of the lag phase duration, is reported as a function of the radius of the SDs. The observed process takes place within a small-volume SD, which, at equilibrium, can be approximated as a hemisphere. The base of the hemisphere is the solution-glass interface, while the remaining surface is the water–oil interface.

Fluorescence microscopy measurements reveal that protein microparticles grow from small structures at fixed points at the drop bottom. Their radius increases over time as shown in Fig. 3. By monitoring the sample drops over the entire volume, at different heights above the glass, the formation of protein microparticles has not been observed. Moreover, during and after their formation, no diffusing species above instrumental resolution are observed in the volume or at the interfaces. These multiple observations confirmed that the process only takes place at the solution-glass interface which, due to the presented experimental protocol, can be manipulated and tuned in terms of the surface area accessible to protein. Notably, the duration of the lag phase in the kinetics is significantly influenced by the SD size (and therefore the accessible surface). On the contrary, the slope of the growth phase does not change significantly within the experimental error (Fig. 5b). This suggests that similar processes occur once a critical nucleus forms at the surface. In this context it is possible to infer that a nucleation process

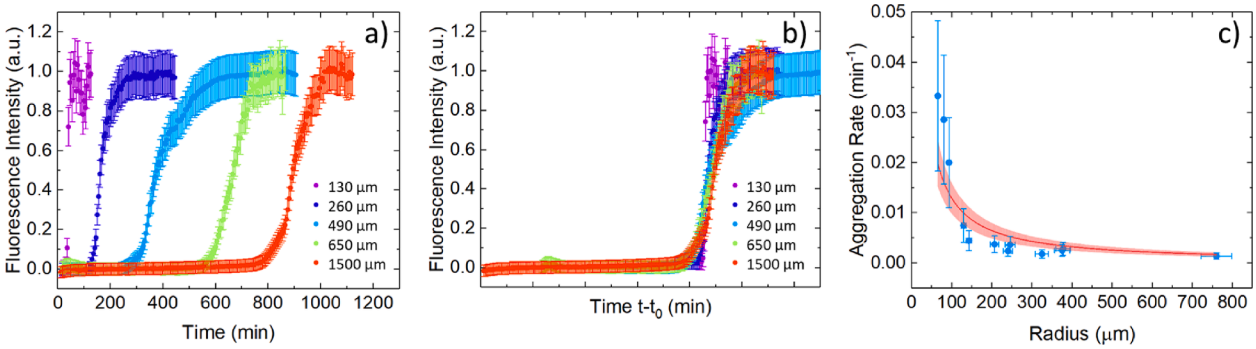

Fig. 5. (a) Time evolution of ThT fluorescence intensity measured in the whole SD, for 5 mg/ml HI in a 20 % Acetic acid solution (pH 1.85) containing 0.5 M NaCl, 0.05 % Tween 20 and 40 mM ThT in SDs with different sizes ranging from 130 μm diameter to 1500 μm diameter. Kinetics presents a sigmoidal profile with a longer lag phase in larger SDs. (b) The same kinetics reported in panel a) overlapped, reveal superimposable profiles. Time has been offset to the lag phase duration of each ThT kinetics. (c) Aggregation rate, measured as the inverse of the lag phase duration, as a function of the SD radius: the lag phase duration was measured as the time for which ThT fluorescence intensity reached 2 % of the maximum fluorescence (plateau region). Data were fitted by the function $y = A+(B/x)$. The fit and the associated error are reported in red.

occurs at the surface, triggering coacervation phenomena. It is well-known that protein molecules display a tendency to aggregate at the surface compared to the bulk. The interaction of proteins with surfaces may decrease the surface energy required for the formation of aggregation nuclei [58,86] which may concur in protein association via multiple mechanisms. Here, experimental data suggest that the observed process is regulated by the attachment of protein molecules to the surface at the bottom of the SD. Attached nucleation [87] where nuclei presence is triggered by protein/surface interactions appears to be a dominant mechanism. After the appearance of nuclei, proteins homogeneously condense around them forming micron-scale particles that exhibit positive staining with ThT. The aggregation rate of the process decreases as the SD radius increases, as shown in Fig. 5c), and it can be associated with the time during which sub-microscopic clusters of proteins form at the bottom of the SD and reach a critical size.

To rationalize the observed behavior, it is possible to consider that the formation of such nuclei on the surface is likely governed by the probability (P) of proteins diffusing within the SD and colliding with the surface. In a simplified description, we can posit that insulin molecules are uniformly distributed in the volume of the hemispherical SD and freely diffuse within it with an average free path λ. Under these assumptions, we can argue that the probability depends on the inverse of the radius of the hemisphere. Indeed, in an oversimplified model where particles freely travel for a length λ and then collide with other particles, the probability for a particle distant $y < \lambda$ from the surface of the SD to impinge the surface itself can be obtained as the ratio between two volumes: the volume of a spherical cap (V_c) of height λ-y and radius λ (the region where the particle would end up after crossing the surface), and the volume of a sphere (V_s) of radius λ (the entire region of points where the particle could end up after traveling a distance λ in an arbitrary direction). Denote such ratio as $P_c(y)$.

Further, the probability (P_L) to find a particle in a layer of thickness dy at distance $y \ll r$ from the SD surface is essentially the ratio between the volume of the layer (V_L) and the entire volume of the hemisphere (V_H),

$$P_L = \frac{V_L}{V_H} = \frac{\pi r^2 dy}{\frac{2\pi r^3}{3}} = \frac{3}{2}\frac{dy}{r}$$

Finally, integration of the product $P_L P_c(y)$ over the interval [0, λ] leads to the final result:

$$P = \int_0^{\lambda} P_c(y) P_L = \int_0^{\lambda} \frac{3}{2r} P_c(y) dy$$

$$P = \frac{9\lambda}{16r}$$

As expected, an inverse relationship exists between the probability P and the radius r, which derives from the SD size in terms of surface-to-volume ratio. This is a heuristic description and is not intended to provide a detailed quantitative analysis. However, in Fig. 5c), we present a fit of the data using a hyperbolic function. We find a reasonable agreement with the experimental data, which supports the idea that attachment nucleation mechanisms occur and are regulated by the free diffusion of insulin molecules. Moreover, the observed condensation phenomenon is nucleated and favored when the surface-to-volume ratio of the SD increases (i.e. smaller radius). This underlines the importance of the surface-to-volume ratio in the observed phenomenon.

Importantly, the observation of aggregation kinetics occurring in SDs of the same size reveals that nucleation sites are heterogeneously distributed on the bottom of the SD at the glass surface level and their number affects the size and the number of the protein particles at the end of the aggregation. A close relation between the number of newly formed supramolecular assemblies and their size exists: at the equilibrium, the number of particles within SDs of the same sizes may vary, as shown in Figure S3. In SDs of the same size a higher number of nucleation sites results in smaller microscale particles in average (see Figure S3 as a reference). This variation may result from the intrinsic variability of the glass surface which determines a different number of nuclei formed at the water–glass interface. Moreover, this could indicate that the same fraction of HI molecules is sequestered within the condensate regardless of the number of nucleation sites, leading to particles of the same spherical morphology, and denoting that the aggregation process is independent of their number.

In Fig. 6a) we report size distributions of HI condensates measured at the end of the kinetics in three representative SDs characterized by the same diameter d = 270 ± 10 μm. In these conditions, identical (within the experimental error) volumes of 5 mg/ml HI solution are incubated at room temperature overnight until the equilibrium is reached and the diameter of fluorescent objects is measured. A 1024 × 1024 pixels representative image of a SD is reported in the inset of the panels. As can be seen in panel 6a), in SDs of the same size, particles are characterized by monodisperse size distributions characterized by different average diameters namely 2.9 ± 1.1 μm (green distribution), 5.0 ± 0.9 μm (yellow distribution) and 6.4 ± 1.5 μm (red distribution).

In Fig. 6b) we report representative size distributions of particles formed in three different SDs with an average diameter of about 1.8 ± 0.1 mm. The inset shows a 1024 × 1024 pixels representative image of the sample with the same scale (50 μm) as the one in panel a). In particular, the size distributions in panel 6b) are centered at 8 ± 2 μm (green distribution), 10 ± 2 μm (yellow distribution) and (9.9 ± 1.5) μm (red distribution), so also in this case a certain variability in the size of the particles is observed, and in average the measured average diameters of the particles are significantly larger than the ones formed in the smaller SD in panel 6a). To better visualize that, two black dotted lines are drawn in correspondence with the centers of the lower diameter distributions (green) for both samples.

A close observation of the data highlights that the average size of the particles increases when the number of particles is reduced, consistent with the constant number of monomers initially in solution. The variation in the measured size of different particles corresponds to the different number of supramolecular structures that grow from fixed nucleation sites observed in the initial stages of the supramolecular assembly. In particular, when a lower number of nuclei occurs the particles grow larger. Therefore, as the experiments are conducted at constant protein concentration, data support the idea that the supramolecular association of HI, in these conditions, ends when the same fraction of HI molecules is recruited in the condensates regardless of their number. Fig. 6c) shows the ratio between the number of pixels where the fluorescent signal is detected and the total number of pixels taking into consideration samples analyzed in panel 6a) and b). This is an estimation of the fraction of the surface occupied by condensates with respect to the total attachment-available surface. The same color code was used to identify the corresponding size distribution in panels a) and b). It is immediately evident that this parameter is constant for SDs of the same size resulting in average 17 % for the 270 μm diameter SD and 45 % for the 1.8 mm diameter SD. This is a further indication that the same fraction of HI molecules is involved in the protein condensation process independently of the number and the size of the final particles in SD of the same size. However, in larger SDs the fraction of occupied area is higher with respect to smaller SDs, which is dictated by the surface-to-volume ratio of the SDs. Indeed, at constant protein concentration, the number of molecules depends on the sample volume (r^3), while the available attached surface depends on (r^2). Since the observed association process occurs at the surface, and the inner volume of the SD serves as a reservoir for molecules, the number of molecules that can be recruited in the condensation process is linearly dependent on the radius.

$$\frac{N}{\Sigma} \propto Cr$$

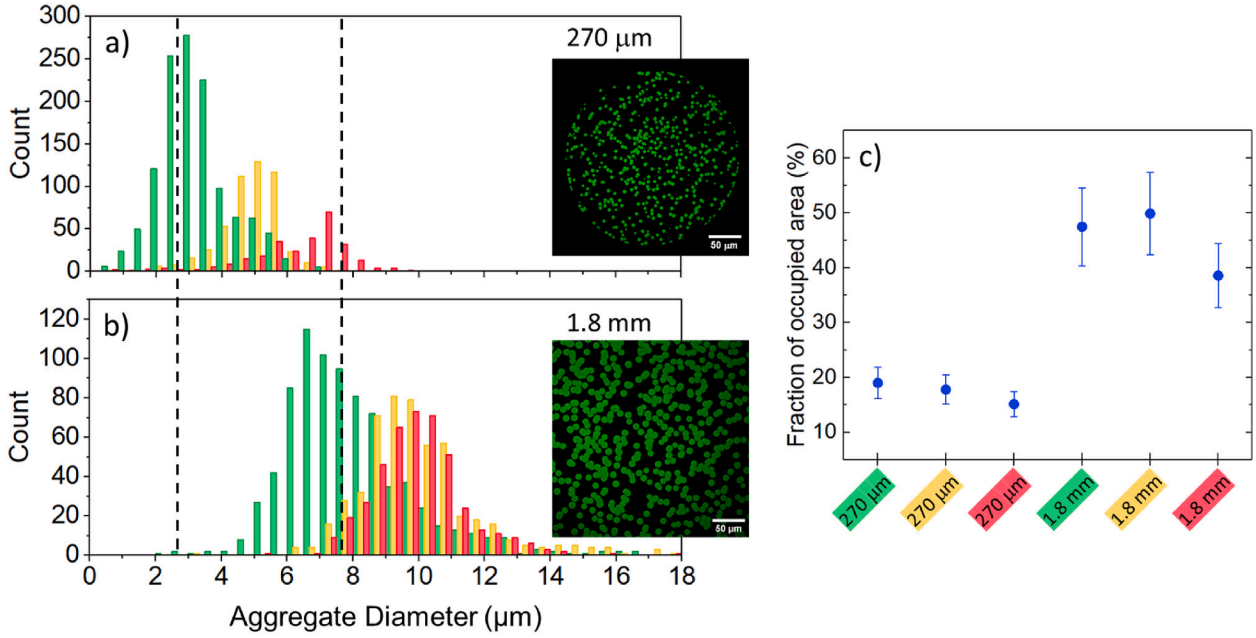

Fig. 6. a) size distributions of particles formed by incubating a 5 mg/ml HI in a 20 % Acetic acid solution (pH 1.85), 0.5 M NaCl, 0.05 % Tween 20 and 40 mM ThT at room temperature overnight in three different aqueous compartments with average diameter 270 ± 10 µm. Histograms bin size is 0.5 µm. The inset shows a 1024 × 1024 pixels representative two-photon microscopy fluorescence image of the HI particles stained with ThT (scale bar 50 µm). Within the same SD particles present the same shape and size but a difference in size is detected in different compartments. The measured average diameter results 2.9 ± 1.1 µm (green distribution), 5.0 ± 0.9 µm yellow distribution and 6.4 ± 1.5 µm (red distribution). b) Size distributions of particles formed in the same solution condition obtained in three different aqueous compartments with average diameter 1.8 mm. Histograms bin size is 0.5 µm. The inset shows a 1024 × 1024 pixels representative two-photon microscopy fluorescence image of the HI particles stained with ThT (scale bar 50 µm). The average measured diameter is 8 ± 2 µm (green distribution), 10 ± 2 µm (yellow distribution) and 9.9 ± 1.5 mm (red distribution). Black dotted vertical lines are used as a guide for the eye allowing to qualitatively observe the different sizes of the particles incubated in SDs with different sizes. c) Ratio between the number of pixels where ThT fluorescence is detected with respect to the one where there is no signal at the end of the supramolecular assembly in SDs with similar sizes. This measures the ratio between the surface occupied by the particles and the total area. The ratios were calculated for the same SDs for which the size distributions were analyzed (legend presents the same color code). The measured ratio is constant at about 17 % and 45 % of the total number of pixels for 270 µm and 1.8 mm SD respectively. This indicates that the same fraction of the glass cover slip is occupied by the particles, independently of their number/size.

where N is the number of molecules, Σ is the accessible surface, C is the concentration and r is the radius of the SD. So, comparing surfaces with the same extension, in a larger SD there is a higher number of molecules available for the growth of the particles, resulting in larger condensates and in a higher fraction of the occupied surface.

Summarizing, the presented experiments allowed us to isolate a supramolecular assembly phenomenon involving HI proteins occurring at the solution-glass interface. Proteins are found to associate within dense spherical condensates positive to ThT with a solid core and a fluid-like corona. The process begins with the formation of small protein clusters/aggregates of HI molecules at the solution-glass interface which serve as nuclei, which are the starting points for phase separation. Once primary nucleation at the interface occurs, proteins gradually separate from the surrounding solution leading to radial growth of the observed microscale coacervates. In difference from what is standardly observed for LLPS the newly formed condensates are not dynamic and remain stable at fixed position around the fixed solid nuclei as shown in experiments reported in Fig. 3, which also allows to exclude the formation of other microscale aggregates in the sample. The evolution of the process brings to hybrid structures and possibly underlying a liquid–solid state transition and the formation of intermolecular β-structures typical of amyloid.

It is possible to gain information on the inter-molecular amyloid β-structure and the spatial heterogeneity of the particles by exploiting the spectroscopic properties of ThT [68]. As reported before, ThT exhibits a remarkable affinity for amyloid fibrils driven by specific interactions with intermolecular β-sheet-rich regions. ThT radiative mechanisms depend on the binding site properties such as charge, presence of specific residues (e.g., aromatics) or spacing between the β-strands [88,89]. Therefore, ThT fluorescence signal exhibits significant variations in both quantum yield and fluorescence lifetime when the dye interacts with structurally diverse amyloid fibrils, enabling the exploration of the polymorphic nature inherent to amyloid aggregates.

In particular, we have previously shown a strict relation between the molecular organization of amyloid-like structures and the ThT fluorescence lifetime by means of Fluorescence Lifetime Imaging Microscopy (FLIM), analyzing the data by means of the phasor approach [68]. FLIM-phasor method allows an estimation of the fluorescence lifetime in each pixel of the image providing a global and graphical representation of the data, without the use of any model [75] (see methods for details). FLIM-Phasor analysis of ThT-stained samples enables the mapping of structural details at a submicron scale, revealing fundamental molecular characteristics such as the degree of β-structure packing [20,68,69,90].

The phasor approach is based on mapping lifetimes onto the phasor plane by applying the Fourier transform to fluorescence decays, without any manipulation of the original data. This allows for a graphical representation of the lifetime data, enabling analysis through a no-fit procedure, which significantly simplifies the process. This is particularly important in the case of complex multi-exponential decays, which further complicate the analysis, as is the case in our study. In such cases, one typically must assume a priori models of fluorescence decay, with the lifetime obtained through a complex function of the parameters describing the measured intensity decay. Conversely, using the phasor method, the model often emerges from the data itself, avoiding incorrect interpretations due to ineffective modeling.

Fig. 7a) shows 256 × 256 pixels representative fluorescence intensity images of particles sample incubated for about 3.5 h in a 220 µm diameter SD at room temperature (scale bar is 10 µm). In Fig. 7b) the

phasor maps obtained from the phasor plot in Fig. 7c) are shown. In Fig. 7d-e) we reported 256 × 256 pixels fluorescence intensity images that focus on individual particles in samples that were incubated overnight at room temperature in SDs measuring 190 μm (d) and 830 μm (e). In Fig. 7f-g) we report the color-coded lifetime fraction maps obtained from the analysis of the corresponding phasor plot in Fig. 7h).

As shown in Fig. 7a), the condensates have a spherical shape as previously observed and their size is about 5 μm in diameter. The phasor analysis reveals a single cluster of pixels located within the universal circle, (Fig. 7c) that stem for a single ThT lifetime distribution characterized by a multi-component lifetime. This observation is in line with what was already observed for ThT in literature where this dye is characterized by a complex fluorescence decay [68,88,91]. To obtain the lifetime map, the lifetime distribution in the phasor plot is selected using a red cursor, and the corresponding are colored in red (phasor maps in Fig. 7b). As can be seen, all the fluorescent particles in the phasor maps result colored in red, indicating that ThT fluorescence lifetime is uniform within the sample. This observation is related to the structural homogeneity of the sample at microscale level.

To explore whether the size of the SDs influences the structure of the particles and to analyze whether the observed ThT fluorescence intensity in Fig. 2d) reflects structural differences within the particles, phasor-FLIM analysis was performed at higher spatial resolution, imaging individual particles formed in SDs of critically different sizes. In the phasor plot presented in Fig. S4e) in SM two distinct and clearly discernible lifetime distributions are evident. The lifetime distribution associated with the longer lifetimes (pink cursor) corresponds to the larger particles incubated in the 830 μm SDs, shown in Fig. 7e), while the distribution linked to the shorter lifetimes (green cursor) is observed in the smaller particles incubated in the 190 μm SDs, shown in Fig. 7d) (refer to Fig. S4c-d) for the phasor maps). This result suggests structural differences between the observed particles at the level of ThT binding sites. Moreover, in phasor maps of the larger particles (Fig. S4d)) it is possible to observe that the core, in correspondence with the lower intensity region, is colored in green. This provides the indication that the core of the particles presents such a molecular organization, that differentiates the core and the edges of the structure, in line with the results reported in Fig. 2. A similar trend is not visible in the smaller particles, since this analysis is limited by the size of the cursors.

Consistent with observations in other amyloid-related systems [20,68,69,90,91], the lifetime distribution clusters extend along a straight line in the phasor plot, connecting two points on the universal circle corresponding to $\tau_1 = 0.6$ ns and $\tau_2 = 2.5$ ns, respectively. This allows us to describe Thioflavin T (ThT) lifetime observed in both samples as double exponential decays, characterized by two primary components with characteristic lifetimes of τ_1 and τ_2. The rapid decay component (τ_1) is attributed to less specific binding sites, where ThT fluorescence arises due to increased environmental viscosity. Conversely, the slower decay component (τ_2) is associated with more specific interactions between ThT and intermolecular β-structures, which impose greater constraints and reduce flexibility within the ThT-binding site, inducing an increase in its quantum yield and lifetime.

A quantitative analysis of the Fluorescence Lifetime Imaging Microscopy (FLIM) data, employing a double exponential model, is performed using the two principal lifetime components according to the equation:

$$I(t) = A_1 e^{\frac{-t}{\tau_1}} + A_2 e^{\frac{-t}{\tau_2}}$$

where A_1 and A_2 are the amplitude of the single exponential decays τ_1 and τ_2. In the phasor plot, the distance between each point of the cloud and the other single exponential phasor is related to the fraction F_1 and F_2 of each component which are proportional to A_1 and A_2. We used an analysis that enables the mapping of fractions F_1 and F_2 in false color (see methods). Specifically, the color scale used ranges from blue, representing the pure fast component with a short lifetime of $\tau_1 = 0.6$ ns, to

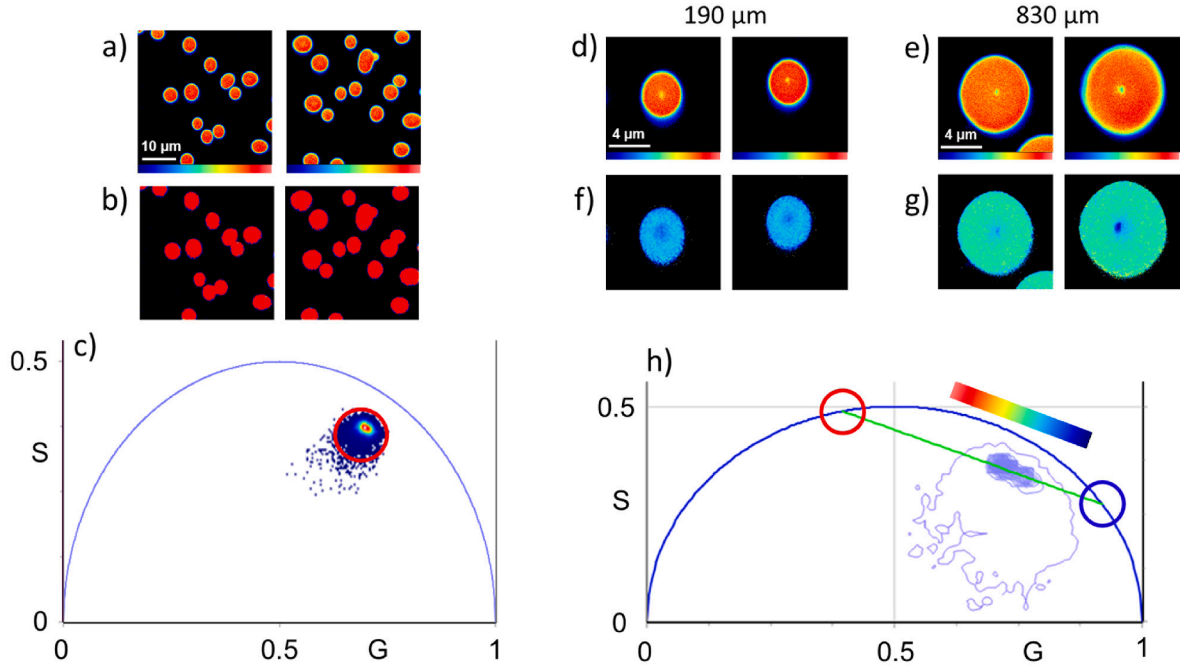

Fig. 7. Phasor analysis of FLIM measurements on particles formed by incubating a 5 mg/ml HI in a 20 % Acetic acid solution (pH 1.85), 0.5 M NaCl, 0.05 % Tween 20 and 40 mM ThT at room temperature. a) 256 × 256 pixels fluorescent intensity images of HI particles incubated in a 220 μm SD for about 3.5 h. Scale bar 10 μm. b) Phasor maps of the previous intensity images: the pixels are colored in red according to the red cursor which selects the single lifetime distribution in the phasor plot (c). d-e) 256 × 256 pixels fluorescent intensity images of single HI particles incubated overnight in a 190 μm SD (d) and 830 μm SD (e). Scale bar 4 μm. f-g) Lifetime fraction maps of the previous intensity image. h) Phasor plot showing an elongated lifetime distribution that lies on a straight line between the two lifetime components, highlighted by the red (longer lifetime) and the blue (shorter lifetime) cursors on the universal circle. The color code is shown above the phasor plot, going from red to blue continuously. The colors of the phasor maps (panel f-g)) follow the color code above the phasor plot.

red, the pure slow component with a long lifetime of $\tau_2 = 2.5$ ns. This color-coded representation provides a visual tool to distinguish and highlight the relative proportions of these two fluorescence components across the analyzed samples. In particular, the shorter lifetime is dominant in the smaller condensates, incubated in the 190 μm SD, with a $F_1 = 0.71$ (light blue), while the larger condensates, incubated in the 830 μm, present a longer lifetime with a $F_1 = 0.62$ (light green). In both samples, it is evident that the shorter lifetime component is dominant, this being in line with the findings from Fluorescence Recovery After Photobleaching (FRAP) measurements. This result indicates that the fluid-like environment surrounding ThT is characterized by binding sites with relatively low specificity for the dye being indicative of their coacervation nature and/or of the presence of a low amount of β-structures within the observed area. Moreover, the analysis suggests that the particles formed in the 190 μm SD have a less densely packed structure in terms of β-sheets, or exhibit lower viscosity compared to those grown in the larger SD where more densely packed intermolecular β-structures are present.

It is important to note that the analysis, using a continuous color map, allows a higher detail in the lifetime map as it is not constrained by the radius of the cursors. For this reason, it is possible to distinguish that in the core of the particles ThT decays are characterized by a shorter fluorescent lifetime (dark blue) with respect to the edge confirming the lower affinity of the particle part in this region for ThT. By examining the phasor plot and comparing the results obtained with what has been previously reported in the literature, we can conclude that the micro-scale particles observed at the solution-glass interface share structural characteristics with naturally occurring amyloid superstructures [35,36,92]. These particles exhibit similarities in shape and size to particulates [39,90,93] and display a core–shell structure, that in our hypothesis arises from primary nucleation, similar to spherulites [68,72]. However, they exhibit relatively weak or sparse intermolecular amyloid β-structures.

4. Conclusions

This study aims to advance our understanding of the factors that initiate the process of amyloid structure formation. This phenomenon represents a critical step in various diseases but, on the bright side, also holds promise as a starting point for the development of new bioinspired sustainable materials. We successfully identified the initial triggers and acquired valuable insights into the subsequent stages of insulin particle formation at the solution-glass interface. In particular, we described a process driven by liquid–liquid phase separation, that leads to the spontaneous formation at room temperature of human insulin amyloid-like particles in sub-microliter scale aqueous sample drops. Interestingly, protein condensation starts from a heterogeneous distribution of nuclei at the surface and occurs almost simultaneously in the whole sample. The presented experimental setup allowed us to highlight a process occurring at the interface which is not energetically favorable as the surface-to-volume ratio decreases. The process is initiated by primary nucleation events occurring at the solution-glass interface and continues via progressive radial size growth of liquid-like condensates.

The formation and growth process, monitored through Thioflavin T fluorescence intensity kinetics at varying spatial resolutions (point, single particle, entire volume of the sample drop) and spectroscopic analysis of Thioflavin T fluorescence signal, indicated a remarkable homogeneity of the process in contrast to the spatiotemporal heterogeneity often observed in the literature for insulin fibril formation at high temperatures [66,67,71]. Nevertheless, similarly to what was reported for high temperature studies [61,69], the interface played a dominant role also in this case. The presence of heterogeneous nuclei was indeed found to control both the number and size of the condensates. Moreover, the surface-to-volume ratio of the sample drop regulates the rate of aggregation kinetics (specifically the lag phase duration) and the size of condensates. Shorter lag phases and smaller condensates are observed when the sample drops possess a higher surface-to-volume ratio. This observation suggests that the probability of individual molecules being recruited into the nuclei is primarily determined by free diffusion.

Finally, we note that the sample volume reduction and the peculiarities of the sample drop size allowed to single out a process which produce particles with amyloid-like nature. Their molecular structure, as shown by FLIM [68], contains few/weak intermolecular β-structures whose content/strength is found to be regulated by the compartment.

The observed protein particles show amyloid-like nature and intriguingly shared features with generic amyloid superstructures obtained in diverse conditions. The size and shape of these structures closely resemble that of protein particulates, and they exhibit a dense solid core enveloped by a fluid-like corona, with a similar architecture to protein spherulites. These observations, again, point out that protein building blocks, when exposed to a range of environmental conditions, exhibit the remarkable ability to form common molecular structures supporting the idea that fundamental and generic laws exist that govern the intricate processes of protein folding and aggregation. These principles transcend environmental variations, emphasizing the robust nature of these biological processes. The identification of such shared traits in protein behavior yields invaluable insights into the fundamental mechanisms that drive protein self-assembly. This understanding is pivotal for unraveling the complexities of protein function and misfolding across diverse biological contexts. Moreover, these insights have the potential for widespread applications, extending beyond basic research to impact various fields where the manipulation of protein structures is significant.

CRediT authorship contribution statement

Giuseppe De Luca: Writing – review & editing, Supervision, Methodology, Data curation, Conceptualization. **Giuseppe Sancataldo:** Writing – review & editing, Supervision, Methodology, Data curation, Conceptualization. **Benedetto Militello:** Writing – review & editing, Methodology, Formal analysis. **Valeria Vetri:** Writing – review & editing, Writing – original draft, Supervision, Resources, Project administration, Methodology, Investigation, Funding acquisition, Formal analysis, Data curation, Conceptualization.

Declaration of competing interest

The authors declare that they have no known competing financial interests or personal relationships that could have appeared to influence the work reported in this paper.

Data availability

Data will be made available on request.

Acknowledgments

The authors thank the University of Palermo (FFR2023) and SiciliAn MicronanOTecH Research And Innovation CEnter “SAMOTHRACE” (MUR, PNRR-M4C2, ECS_00000022), spoke 3 - Università degli Studi di Palermo S2-COMMs - Micro and Nanotechnologies for Smart & Sustainable Communities, for financial support.

Appendix A. Supplementary data

Supplementary data to this article can be found online at https://doi.org/10.1016/j.jcis.2024.07.135.

References

[1] S. Alberti, A. Gladfelter, T. Mittag, Considerations and Challenges in Studying Liquid-Liquid Phase Separation and Biomolecular Condensates, Cell 176 (2019) 419–434. Preprint at 10.1016/j.cell.2018.12.035.

[2] S.F. Banani, H.O. Lee, A.A. Hyman, M.K. Rosen, Biomolecular condensates: Organizers of cellular biochemistry, Nat. Rev. Mol. Cell Biol. 18 (2017) 285–298. Preprint at 10.1038/nrm.2017.7.

[3] E.M. Courchaine, A. Lu, K.M. Neugebauer, Droplet organelles? EMBO J 35 (2016) 1603–1612.

[4] C. Alfano, et al., Molecular Crowding: The History and Development of a Scientific Paradigm, Chem Rev (2024).

[5] A. Molliex, et al., Phase Separation by Low Complexity Domains Promotes Stress Granule Assembly and Drives Pathological Fibrillization, Cell 163 (2015).

[6] W.M. Babinchak, W.K. Surewicz, Liquid-Liquid Phase Separation and Its Mechanistic Role in Pathological Protein Aggregation, J. Mol. Biol. 432 (2020), https://doi.org/10.1016/j.jmb.2020.03.004.

[7] E.W. Martin, et al., A multi-step nucleation process determines the kinetics of prion-like domain phase separation, Nat Commun 12 (2021).

[8] N.M. Kanaan, C. Hamel, T. Grabinski, B. Combs, Liquid-liquid phase separation induces pathogenic tau conformations in vitro, Nat Commun 11 (2020).

[9] S.S. Ribeiro, N. Samanta, S. Ebbinghaus, J.C. Marcos, The synergic effect of water and biomolecules in intracellular phase separation, Nat. Rev. Chem. 3 (2019), https://doi.org/10.1038/s41570-019-0120-4.

[10] G. Krainer, et al., Reentrant liquid condensate phase of proteins is stabilized by hydrophobic and non-ionic interactions, Nat Commun 12 (2021).

[11] M. Moron, et al., Gelation Dynamics upon Pressure-Induced Liquid-Liquid Phase Separation in a Water-Lysozyme Solution, J. Phys. Chem. B 126 (2022) 4160–4167.

[12] A. Testa, et al., Sustained enzymatic activity and flow in crowded protein droplets, Nat Commun 12 (2021).

[13] S. Park, et al., Dehydration entropy drives liquid-liquid phase separation by molecular crowding, Commun Chem 3 (2020).

[14] S. Da Vela, et al., Kinetics of liquid-liquid phase separation in protein solutions exhibiting LCST phase behavior studied by time-resolved USAXS and VSANS, Soft Matter 12 (2016) 9334–9341.

[15] F. Zhang, et al., Universality of protein reentrant condensation in solution induced by multivalent metal ions, Proteins Struct. Funct. Bioinf. 78 (2010) 3450–3457.

[16] Hyman, A. A., Weber, C. A. & Jülicher, F. Liquid-liquid phase separation in biology. Annual review of cell and developmental biology vol. 30 39–58 Preprint at 10.1146/annurev-cellbio-100913-013325 (2014).

[17] Gomes, E. & Shorter, J. The molecular language of membraneless organelles. Journal of Biological Chemistry vol. 294 7115–7127 Preprint at 10.1074/jbc.TM118.001192 (2019).

[18] C.P. Brangwynne, P. Tompa, R.V. Pappu, Polymer physics of intracellular phase transitions, Nat Phys 11 (2015).

[19] A.C. Murthy, et al., Molecular interactions underlying liquid–liquid phase separation of the FUS low-complexity domain, Nat Struct Mol Biol 26 (2019).

[20] M.A. Morando, et al., Solution structure of recombinant Pvfp-5β reveals insights into mussel adhesion, Commun Biol 5 (2022).

[21] Muiznieks, L. D., Sharpe, S., Pomès, R. & Keeley, F. W. Role of Liquid–Liquid Phase Separation in Assembly of Elastin and Other Extracellular Matrix Proteins. Journal of Molecular Biology vol. 430 4741–4753 Preprint at 10.1016/j.jmb.2018.06.010 (2018).

[22] Y. Xing, et al., Amyloid Aggregation under the Lens of Liquid-Liquid Phase Separation, J. Phys. Chem. Lett. 12 (2021).

[23] G.A.P. de Oliveira, Y. Cordeiro, J.L. Silva, T.C.R.G. Vieira, Liquid-liquid phase transitions and amyloid aggregation in proteins related to cancer and neurodegenerative diseases, Adv Protein Chem Struct Biol 118 (2019).

[24] D.T. Murray, et al., Structure of FUS Protein Fibrils and Its Relevance to Self-Assembly and Phase Separation of Low-Complexity Domains, Cell 171 (2017).

[25] X. Gui, et al., Liquid–liquid phase separation of amyloid-β oligomers modulates amyloid fibrils formation, J. Biol. Chem. 299 (2023).

[26] S. Sudhakar, A. Manohar, E. Mani, Liquid-Liquid Phase Separation (LLPS)-Driven Fibrilization of Amyloid-β Protein, ACS Chem Neurosci (2023), https://doi.org/10.1021/acschemneuro.3c00286.

[27] Y. Lin, Y. Fichou, Z. Zeng, N.Y. Hu, S. Han, Electrostatically Driven Complex Coacervation and Amyloid Aggregation of Tau Are Independent Processes with Overlapping Conditions, ACS Chem Neurosci 11 (2020).

[28] S. Ambadipudi, J. Biernat, D. Riedel, E. Mandelkow, M. Zweckstetter, Liquid-liquid phase separation of the microtubule-binding repeats of the Alzheimer-related protein Tau, Nat Commun 8 (2017).

[29] L. Pytowski, C.F. Lee, A.C. Foley, D.J. Vaux, L. Jean, Liquid-liquid phase separation of type II diabetes-associated IAPP initiates hydrogelation and aggregation, Proc Natl Acad Sci U S A 117 (2020).

[30] Y. Shen, et al., Biomolecular condensates undergo a generic shear-mediated liquid-to-solid transition, Nat Nanotechnol 15 (2020).

[31] Q. Guo, et al., Hydrogen-bonds mediate liquid-liquid phase separation of mussel derived adhesive peptides, Nat Commun 13 (2022).

[32] S. Ranganathan, E. Shakhnovich, The physics of liquid-to-solid transitions in multi-domain protein condensates, Biophys J 121 (2022).

[33] W.M. Babinchak, et al., The role of liquid-liquid phase separation in aggregation of the TDP-43 low-complexity domain, J. Biol. Chem. 294 (2019).

[34] B. Wolozin, P. Ivanov, Stress granules and neurodegeneration. Nature Reviews Neuroscience vol. 20 Preprint at 10.1038/s41583-019-0222-5 (2019).

[35] V. Vetri, V. Foderà, The route to protein aggregate superstructures: Particulates and amyloid-like spherulites. FEBS Letters vol. 589 2448–2463 Preprint at 10.1016/j.febslet.2015.07.006 (2015).

[36] Krebs, M. R. H., Domike, K. R. & Donald, A. M. Protein aggregation: More than just fibrils. in *Biochemical Society Transactions* vol. 37 (2009).

[37] K.R. Domike, A.M. Donald, Thermal dependence of thermally induced protein spherulite formation and growth: Kinetics of β-lactoglobulin and insulin, Biomacromolecules 8 (2007) 3930–3937.

[38] J. Adamcik & R. Mezzenga, Amyloid Polymorphism in the Protein Folding and Aggregation Energy Landscape. Angewandte Chemie - International Edition vol. 57 Preprint at 10.1002/anie.201713416 (2018).

[39] V. Foderà, et al., Observation of the early structural changes leading to the formation of protein superstructures, J. Phys. Chem. Lett. 5 (2014) 3254–3258.

[40] M.R.H. Krebs, E.H.C. Bromley, S.S. Rogers, A.M. Donald, The mechanism of amyloid spherulite formation by bovine insulin, Biophys J 88 (2005).

[41] H. Tange, et al., Liquid liquid phase separation of full-length prion protein initiates conformational conversion in vitro, J. Biol. Chem. 296 (2021).

[42] E. Trilisky, R. Gillespie, T.D. Osslund, S. Vunnum, Crystallization and liquid-liquid phase separation of monoclonal antibodies and fc-fusion proteins: Screening results, Biotechnol Prog 27 (2011).

[43] S. Tanaka, M. Yamamoto, K. Ito, R. Hayakawa, M. Ataka, Relation between the phase separation and the crystallization in protein solutions, Phys Rev E Stat Phys Plasmas Fluids Relat Interdiscip Topics 56 (1997).

[44] R. Dec, M.W. Jaworek, W. Dzwolak, R. Winter, Liquid-Droplet-Mediated ATP-Triggered Amyloidogenic Pathway of Insulin-Derived Chimeric Peptides: Unraveling the Microscopic and Molecular Processes, J Am Chem Soc (2022), https://doi.org/10.1021/jacs.2c12611.

[45] Cohen, S. I. A., Vendruscolo, M., Dobson, C. M. & Knowles, T. P. J. From macroscopic measurements to microscopic mechanisms of protein aggregation. Journal of Molecular Biology vol. 421 Preprint at 10.1016/j.jmb.2012.02.031 (2012).

[46] K.E. Routledge, G.G. Tartaglia, G.W. Platt, M. Vendruscolo, S.E. Radford, Competition between Intramolecular and Intermolecular Interactions in an Amyloid-Forming Protein, J Mol Biol 389 (2009).

[47] A.J. Modler, K. Gast, G. Lutsch, G. Damaschun, Assembly of amyloid protofibrils via critical oligomers - A novel pathway of amyloid formation, J Mol Biol 325 (2003).

[48] T.R. Jahn, S.E. Radford, Folding versus aggregation: Polypeptide conformations on competing pathways. Archives of Biochemistry and Biophysics vol. 469 Preprint at 10.1016/j.abb.2007.05.015 (2008).

[49] S.M. Vaiana, M.B. Palma-Vittorelli, M.U. Palma, Time scale of protein aggregation dictated by liquid-liquid demixing, Proteins Struct. Funct. Genet. 51 (2003).

[50] M. Manno, et al., Multiple interactions between molecular and supramolecular ordering, Phys Rev E Stat Phys Plasmas Fluids Relat Interdiscip Topics 59 (1999).

[51] F. Pullara, A. Emanuele, M.B. Palma-Vittorelli, M.U. Palmay, Protein aggregation/crystallization and minor structural changes: Universal versus specific aspects, Biophys J 93 (2007).

[52] S. Da Vela, et al., Arrested and temporarily arrested states in a protein-polymer mixture studied by USAXS and VSANS, Soft Matter 13 (2017).

[53] J. Van Lindt, et al., A generic approach to study the kinetics of liquid–liquid phase separation under near-native conditions, Commun Biol 4 (2021).

[54] A. Strofaldi, M.K. Quinn, A.M. Seddon, J.J. McManus, Polymorphic protein phase transitions driven by surface anisotropy, J. Chem. Phys. 158 (2023).

[55] V. Sluzky, A.M. Klibanov, R. Langer, Mechanism of insulin aggregation and stabilization in agitated aqueous solutions, Biotechnol Bioeng 40 (1992).

[56] V. Sluzky, J.A. Tamada, A.M. Klibanov, R. Langer, Kinetics of insulin aggregation in aqueous solutions upon agitation in the presence of hydrophobic surfaces, Proc Natl Acad Sci U S A 88 (1991).

[57] S. Li, R.M. Leblanc, Aggregation of insulin at the interface, J. Phys. Chem. B 118 (2014).

[58] F. Grigolato, P. Arosio, The role of surfaces on amyloid formation, Biophys Chem 270 (2021).

[59] Z. Toprakcioglu, et al., Adsorption free energy predicts amyloid protein nucleation rates, Proc Natl Acad Sci U S A 119 (2022).

[60] S. Campioni, et al., Interfaces Determine the Fate of Seeded α-Synuclein Aggregation, Adv Mater Interfaces 7 (2020).

[61] X. Zhou, et al., Heterogeneous and Surface-Catalyzed Amyloid Aggregation Monitored by Spatially Resolved Fluorescence and Single Molecule Microscopy, J. Phys. Chem. Lett. 14 (2023).

[62] N. Katina, A. Mikhaylina, N. Ilina, I. Eliseeva, V. Balobanov, Near-wall aggregation of amyloidogenic aβ 1–40 peptide: Direct observation by the fret, Molecules 26 (2021).

[63] J. Brange, L. Langkjœr, Insulin Structure and Stability. in Stability and Characterization of Protein and Peptide Drugs (eds. Wang, Y. J. & Pearlman Rodney) vol. vol 5 315–350 (Springer, Boston, MA, 1993).

[64] D. Rimmerman, et al., Direct Observation of Insulin Association Dynamics with Time-Resolved X-ray Scattering, J. Phys. Chem. Lett. 8 (2017) 4413–4418.

[65] C. Bryant, et al., Acid Stabilization of Insulin, Biochemistry 32 (1993).

[66] V. Foderà, F. Librizzi, M. Groenning, M. Van De Weert, M. Leone, Secondary nucleation and accessible surface in insulin amyloid fibril formation, J. Phys. Chem. B 112 (2008) 3853–3858.

[67] V. Foderà, et al., Self-organization pathways and spatial heterogeneity in insulin amyloid fibril formation, J. Phys. Chem. B 113 (2009).

[68] G. De Luca, et al., Probing ensemble polymorphism and single aggregate structural heterogeneity in insulin amyloid self-assembly, J Colloid Interface Sci 574 (2020).

[69] X. Zhou, et al., Polysorbate 80 controls Morphology, structure and stability of human insulin Amyloid-Like spherulites, J Colloid Interface Sci 606 (2022) 1928–1939.
[70] T. Sneideris, et al., PH-driven polymorphism of insulin amyloid-like fibrils, PLoS One 10 (2015).
[71] M. Mauro, et al., Kinetics of Different Processes in Human Insulin Amyloid Formation, J Mol Biol 366 (2007) 258–274.
[72] M.I. Smith, V. Foderà, J.S. Sharp, C.J. Roberts, A.M. Donald, Factors affecting the formation of insulin amyloid spherulites, Colloids Surf B Biointerfaces 89 (2012) 216–222.
[73] M. Bouchard, J. Zurdo, E.J. Nettleton, C.M. Dobson, C.V. Robinson, Formation of insulin amyloid fibrils followed by FTIR simultaneously with CD and electron microscopy, Protein Sci. 9 (2000).
[74] W. Dzwolak, R. Ravindra, J. Lendermann, R. Winter, Aggregation of bovine insulin probed by DSC/PPC calorimetry and FTIR spectroscopy, Biochemistry 42 (2003).
[75] M.A. Digman, V.R. Caiolfa, M. Zamai, E. Gratton, The phasor approach to fluorescence lifetime imaging analysis, Biophys J 94 (2008).
[76] J.C. Baret, Surfactants in droplet-based microfluidics. Lab on a Chip vol. 12 Preprint at 10.1039/c1lc20582j (2012).
[77] G. Arrabito, et al., Monitoring few molecular binding events in scalable confined aqueous compartments by raster image correlation spectroscopy (CADRICS), Lab Chip 16 (2016) 4666–4676.
[78] G. Arrabito, et al., Printing Life-Inspired Subcellular Scale Compartments with Autonomous Molecularly Crowded Confinement, Adv Biosyst 3 (2019).
[79] B.Y. Feng, B.K. Shoichet, A detergent-based assay for the detection of promiscuous inhibitors, Nat Protoc 1 (2006).
[80] H. Knoch, et al., Complex Micellization Behavior of the Polysorbates Tween 20 and Tween 80, Mol Pharm 18 (2021).
[81] A. Patist, S.S. Bhagwat, K.W. Penfield, P. Aikens, D.O. Shah, On the measurement of critical micelle concentrations of pure and technical-grade nonionic surfactants, J Surfactants Deterg 3 (2000).
[82] S. Linse, Monomer-dependent secondary nucleation in amyloid formation. Biophysical Reviews vol. 9 329–338 Preprint at 10.1007/s12551-017-0289-z (2017).
[83] S.I.A. Cohen, et al., Proliferation of amyloid-β42 aggregates occurs through a secondary nucleation mechanism, Proc Natl Acad Sci U S A 110 (2013) 9758–9763.
[84] P. Arosio, M. Beeg, L. Nicoud, M. Morbidelli, Time evolution of amyloid fibril length distribution described by a population balance model, Chem Eng Sci 78 (2012) 21–32.
[85] V. Vetri, et al., Ethanol Controls the Self-Assembly and Mesoscopic Properties of Human Insulin Amyloid Spherulites, J. Phys. Chem. B 122 (2018).
[86] A.K. Srivastava, et al., β-Amyloid aggregation and heterogeneous nucleation, Protein Sci. 28 (2019), https://doi.org/10.1002/pro.3674. Preprint at 2019.
[87] L. Tumbek, A. Winkler, Attachment limited versus diffusion limited nucleation of organic molecules: Hexaphenyl on sputter-modified mica, Surf Sci 606 (2012).
[88] A.I. Sulatskaya, A.V. Lavysh, A.A. Maskevich, I.M. Kuznetsova, K.K. Turoverov, Thioflavin T fluoresces as excimer in highly concentrated aqueous solutions and as monomer being incorporated in amyloid fibrils, Sci Rep 7 (2017).
[89] Biancalana, M. & Koide, S. Molecular mechanism of Thioflavin-T binding to amyloid fibrils. Biochimica et Biophysica Acta - Proteins and Proteomics vol. 1804 Preprint at 10.1016/j.bbapap.2010.04.001 (2010).
[90] D. Fennema Galparsoro, et al., Conformational Transitions upon Maturation Rule Surface and pH-Responsiveness of α-Lactalbumin Microparticulates, ACS Appl Bio Mater 4 (2021).
[91] A.J. Thompson, et al., Molecular Rotors Provide Insights into Microscopic Structural Changes during Protein Aggregation, J. Phys. Chem. B 119 (2015).
[92] C. Thorlaksen, M.B. Neergaard, M. Groenning, V. Foderà, Reproducible Formation of Insulin Superstructures: Amyloid-Like Fibrils, Spherulites, and Particulates, Methods Mol. Biol. vol. 2551 (2023).
[93] M.R.H. Krebs, G.L. Devlin, A.M. Donald, Protein particulates: Another generic form of protein aggregation? Biophys J 92 (2007).